DOI: 10.1039/C9TC06928C

Black arsenene as a promising anisotropic sensor with high sensitivity and selectivity: insights from a first-principles investigation

Jianjun Mao[1] and Yue Chen[1,2,*]

[1]*Department of Mechanical Engineering, The University of Hong Kong, Pokfulam Road, Hong Kong SAR, China*

[2]*HKU Shenzhen Institute of Research and Innovation, Yuexing 2nd Road, Nanshan, Shenzhen 518057, China*

†Electronic supplementary information (ESI) available.

Abstract:

Black arsenene (B-As), a monolayer of arsenic, is of general interest due to its considerable bandgap, high carrier mobility, anisotropic nature and ideal stability under ambient conditions. In the present study, the adsorption of NH_3, CO, CO_2, NO, and NO_2 on B-As was investigated using first-principles simulations to exploit the potential of B-As as a gas sensor. The binding strengths between the molecules and B-As were uncovered and could be modulated by a vertical electric field due to charge transfer variations but were insensitive to equibiaxial tensile strain. Our results show that B-As is more sensitive to nitrogen-containing gases. We further investigated the current-voltage (*I-V*) relationship using the nonequilibrium Green's function (NEGF) formalism. The transport features show large anisotropy along different directions (armchair and zigzag), which is consistent with the anisotropic band structure of B-As. Interestingly, the *I-V* relationship exhibits distinct responses with a marked change of the *I-V* curves along either the armchair or zigzag directions depending on the type of molecule. Spin polarized currents after the adsorptions of NO and NO_2 were also obtained, which indicates that B-As has superior wide-range application as a gas sensor.

Key words: Arsenene, Gas sensor, Anisotropic transport, Spin polarized currents, Electric field, Strain

* Corresponding author. Email: yuechen@hku.hk

Introduction

Sensitive and selective solid-state gas sensors with low production costs and miniature sizes are in high demand for monitoring environmental pollution and agricultural and specific medical applications [1, 2]. After the isolation of graphene [3], the last decade has witnessed an unprecedented interest in its emerging new allotropes or other 2D materials and their various potential applications [4-6]. Their high surface-to-volume ratio, ultimate exposure of surface atoms and high sensitivity to subtle changes in the surroundings mean 2D nanomaterials show great promise for various sensing systems [7-9]. It was already reported that graphene-based sensors can detect even individual molecules [10]. Recently, group V elemental monolayers (P, As, Sb, and Bi) have attracted tremendous attention due to their considerable bandgaps and high carrier mobilities [11-16]. In addition, black phosphorene (B-P) was initially predicted to be a better gas sensing material than graphene and monolayer MoS_2 by a first-principles study [17] and was experimentally verified [18, 19]. Unfortunately, B-P can easily degrade under ambient conditions via oxidation, which severely restricts its prospective applications [20, 21]. Recently, a metastable allotrope, blue phosphorene (β-P), was shown to be a suitable candidate for gas detectors [22]. After the exfoliation of phosphorene (B-P or α-P) [12], antimonene (β-Sb) has also been obtained on Bi_2Te_3 and Sb_2Te_3 [23]. Moreover, a multilayer grey arsenene (β-As) nanoribbon was synthesized on an InAs substrate using a plasma-assisted process [24]. Additionally, β-As showed an impressive sensing ability for NO and NO_2 [25].

As a competing metastable phase, layered black arsenic (B-As) was first predicted theoretically [26] and then synthesized in the lab [27, 28]. B-As exhibits interesting properties, including tunable bandgaps [26, 29], low lattice thermal conductivities [30], high in-plane anisotropies [26, 27, 30], and possible transitions and hybridizations with other 2D As allotropes [31]. B-As has a similar structural configuration as B-P and has excellent physical and chemical stabilities [27, 28, 32]. However, studies about the transport properties

and sensor application of B-As are still lacking. Recently, monolayer and few-layer B-As-based FETs have been fabricated, and their unique transport characteristics were revealed [28]. To exploit the possibilities of gas sensors based on single-layer B-As, systematic fundamental studies are essential for understanding the interaction between B-As and adsorbates.

In this work, we investigated the structural and electronic properties of the adsorption of NH_3, CO, CO_2, NO, and NO_2 on single-layer B-As using first-principles calculations. Preferential adsorption positions, adsorption energies, and charge transfers were determined. We demonstrate that the binding strengths of these gas molecules are between those for physical and chemical adsorption, which may allow the material to be recycled as a gas sensor. Our results also show that the strength of binding is related to the amount of charge transfer between the molecules and B-As. In addition, the interaction between NO or NO_2 and B-As can be tuned easily by an electric field; however, it is relatively insensitive to equibiaxial tensile strain. Realization of a practical device technology will require a detailed understanding of the transport mechanisms. We then calculated the *I-V* relation of B-As without and with gas molecule adsorption using a non-equilibrium Green's function (NEGF) formalism. The results not only show sensitive changes to adsorption but also exhibit remarkably high selectivity for different gas molecules that may induce variations in transport behaviour along either the armchair or zigzag direction of B-As. In addition, spin-resolved transport properties can be generated after the adsorption of NO and NO_2. The combined sensitivity and selectivity of the *I-V* relation to the adsorption of various gas molecules make B-As a promising candidate for high-performance sensing applications.

Model and method

Structure optimization and electronic structure calculations were performed with the generalized gradient approximation (GGA) in the parametrization of Perdew-Burke-Ernzerhorf (PBE) using the plane-wave basis Vienna ab initio simulation package (VASP) [33, 34]. As-$4s^2 4p^3$, C-$2s^2 2p^2$, O-$2s^2 2p^4$, N-$2s^2 2p^3$, and H-1s were treated as

valance electrons, while the ionic cores were represented by the projector augmented wave (PAW) potentials. The Kohn-Sham orbitals were expanded using plane waves with a well-converged cutoff energy of 500 eV. The Brillouin zone integrations were performed with a *k*-point density of 2π ×0.03 $Å^{-1}$ adopting the Γ-centred Monkhorst-Pack scheme. In the calculation, we chose a 3 × 3 supercell to simulate the periodic structure of B-As, and a large vacuum region of 15 Å in the *z* direction was applied and dipole corrections were employed. The convergence criteria for the electronic self-consistent iteration and the ionic relaxation loop were set to 10^{-5} eV and 0.01 eV/Å, respectively. We included a semiempirical DFT-D2 type of dispersion correction as the long-range interaction between B-As and the gas molecules [35]. The electric field was applied perpendicular to the B-As plane in the *z* direction. Spin polarization was included in all calculations.

The adsorption energy (E_{ads}) of the gas molecule was defined as $E_{ads} = E_{As+gas} - E_{As} - E_{gas}$, where E_{As+gas}, E_{As}, and E_{gas} are the total energies of the gas-adsorbed B-As, pristine B-As and gas molecules, respectively. Accordingly, the charge density difference (CDD) was evaluated by $\Delta\rho = \rho_{As+gas} - \rho_{As} - \rho_{gas}$; here, the charge density of bare B-As (ρ_{As}) and an isolated gas molecule (ρ_{gas}) were computed with the same coordination as that in the gas adsorbed configuration (ρ_{As+gas}). Bader charge analysis [36] was performed to evaluate the charge transfer. The electronic transport properties were studied by the NEGF techniques within the Keldysh formalism as implemented in the TranSIESTA package [37]. The electric current through the contact region was calculated using the Landauer−Buttiker formula [38]: $I(V) = G_0\int_{\mu_R}^{\mu_L} T(E, V)dE$, where $G_0=2(e^2/h)$ is the unit of the quantum conductance and $T(E, V)$ is the transmission probability of electronic incident at energy E under a potential bias V. The electrochemical potential difference between the left and right electrode is $eV=\mu_R-\mu_L$.

Results and discussion

As shown in Figure 1, a 3 × 3 B-As supercell with lattice dimensions of 11.064 Å × 14.253 Å, corresponding to a unit cell of 3.688 Å × 4.751 Å, was used to simulate the

adsorption of NH_3, CO, CO_2, NO, and NO_2. The boundary structure is anisotropic along the *x* and *y* directions, labelled as the armchair and zigzag directions, respectively. The preferred adsorption sites of these gas molecules, as illustrated in Figure 1, were determined within various adsorption sites and molecular orientations (either parallel or vertical to the substrate), as shown in Figure S1 in the ESI. The key adsorption parameters regarding the adsorption energies, adsorption heights, and bond lengths of adsorbed gas molecules are summarized in Table 1. For the NH_3 molecule, the N atom is located at the centre of the puckered honeycomb structure with an adsorption distance of 2.31 Å, as shown in Figure 1 (a. f). The CO molecule also stays above the B-As with the C atom located at the centre of the honeycomb; however, the C atom of CO_2 is located at the middle of As-As bonding. Compared with NH_3, CO and CO_2 molecules are higher above B-As with adsorption distances of 2.83 Å and 2.99 Å, respectively. However, for NO and NO_2, they prefer to adsorb near the top of the As atom with a shorter distance (NO: 2.19 Å; NO_2: 2.24 Å), as shown in Figure 1.

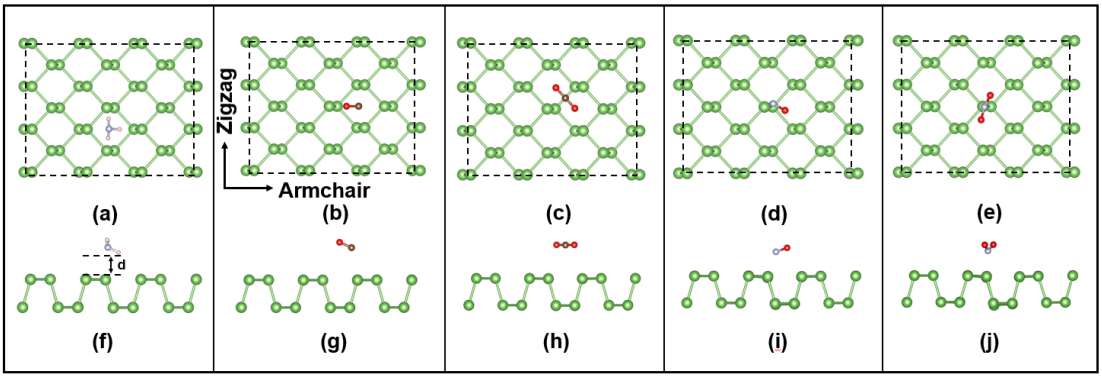

Figure 1 (colour online) Top views (a-e) and side views (f-j) of the optimized structures of B-As with NH_3, CO, CO_2, NO, and NO_2 adsorption. The green, cyan, pink, red, and brown spheres represent As, N, H, O, and C atoms, respectively. The distance *d* between the gas molecule and B-As is indicated in (f).

For a quantitative description of the gas adsorption strength on B-As, the adsorption energies are listed in Table 1. CO has the weakest adsorption strength (-0.14 eV), while NO_2 has the strongest (-0.34 eV) among the gas molecules we studied. In addition, the values for NH_3, CO_2, and NO adsorption are -0.26, -0.16, and -0.33 eV, respectively. Similar to MoS_2 [39, 40], graphene [10], and phosphorene [17] in their potential use as gas

sensors, all of the adsorption energies with B-As are large enough to withstand the thermal disturbances at room temperature that are on the energy scale of k_bT (approximately 25.7 meV at 298 K; k_b is the Boltzmann constant). Obviously, NH_3, NO, and NO_2 have larger adsorption energies than CO and CO_2, indicating that B-As is more sensitive to nitrogen-containing gases; a similar situation was also found in two-dimensional MoS_2 [39, 40] and phosphorene [17]. In addition, the gas adsorption strength on B-As is comparable to that of phosphorene [41] but stronger than that of graphene [42] and MoS_2 [39, 40], suggesting a higher level of sensitivity for gas adsorption on B-As.

Previous studies on gas adsorption have confirmed the important role of charge transfer in the adsorption strength and resistance of a substrate [17]. The charge transfer induced by gas molecule adsorption can be used for highly sensitive sensors, even with the possibility of detecting an individual molecule [10], where the sensor property is based on changes in the resistivity with the gas molecules acting as donors or acceptors. It is expected that the electrical resistivity of B-As will also be influenced by gas molecule adsorption. Therefore, we performed Bader charge analysis for these adsorption systems, and the results are summarized in Table 1. For NH_3 adsorption on B-As, there is only a small amount of charge transfer (0.02 e) from the NH_3 molecule to the substrate. In contrast, CO, CO_2, NO, and NO_2 are all accepters, and more significant charge transfers are observed in NO and NO_2. Larger charge transfer is expected to induce more significant changes in the conductivity of the system. The charge transfer can also be visualized by the charge density difference (CDD), as shown in Figure 2 (a-e). The charge depletion and accumulation regions are more prominent around NO and NO_2, which is in agreement with the Bader charge analysis.

Table 1. Adsorption parameters including the adsorption energy (E_{ads}), magnetism (*Mag*), Bader charge transfer (Q) with positive values standing for accepting electrons, the bond length of the adsorbate (L), and the nearest distance (d) between the gas molecule and B-As

	NH_3	CO	CO_2	NO	NO_2
E_{ads} (eV)	-0.26	-0.14	-0.16	-0.33	-0.34
Mag (μ_B)	0	0	0	0.95	0.26
Q (e)	-0.02	0.03	0.04	0.23	0.44

L (Å)	1.023/1.021	1.15	1.18	1.19	1.23
d (Å)	2.31	2.83	2.99	2.19	2.24

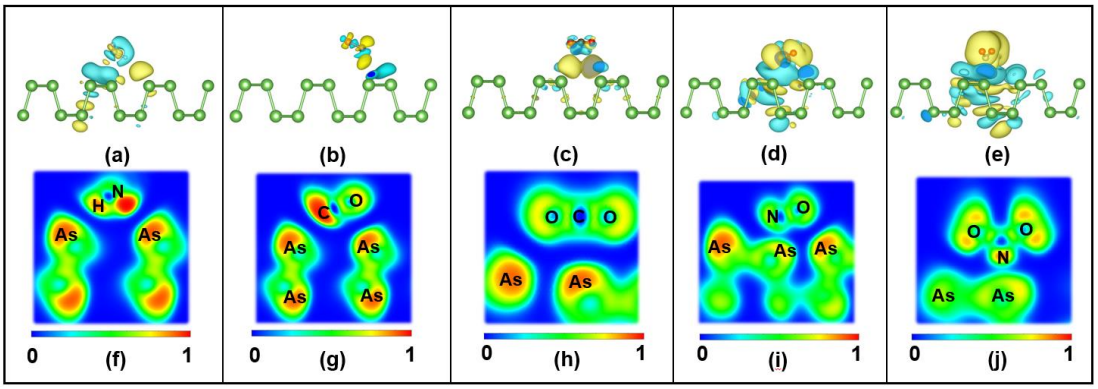

Figure 2 (colour online) Charge density difference (CDD) plots for (a) NH_3, (b) CO, (c) CO_2, (d) NO, and (e) NO_2 adsorbed on B-As. The yellow (blue) distribution corresponds to charge accumulation (depletion). The isosurface value is equal to 0.0003 e$Å^{-3}$. Electron localization function (ELF) of (f) NH_3, (g) CO, (h) CO_2, (i) NO, and (j) NO_2 adsorbed on B-As.

The ELF of the adsorption systems, as shown in Figure 2 (f-j), indicates a stronger interaction between N-based gases (NO and NO_2) and B-As and clearly shows the lack of electron sharing between gas molecules and the B-As sheet. This indicates that sensing with the B-As substrate for these gas molecules may be reversible.

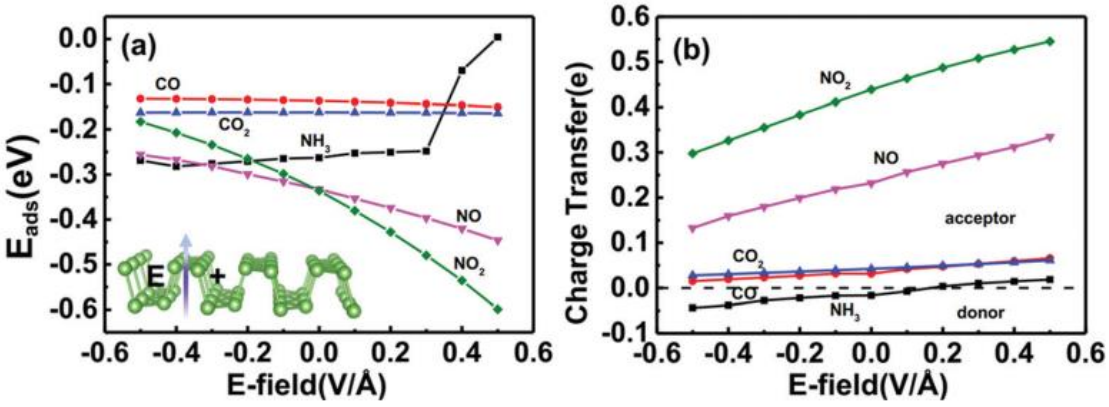

Figure 3 Variations of the calculated adsorption energy (a) and charge transfer (b) as a function of an external electric field for NH_3, CO, CO_2, NO, and NO_2. The positive direction "+" of the *E* field is illustrated in the inset of (a).

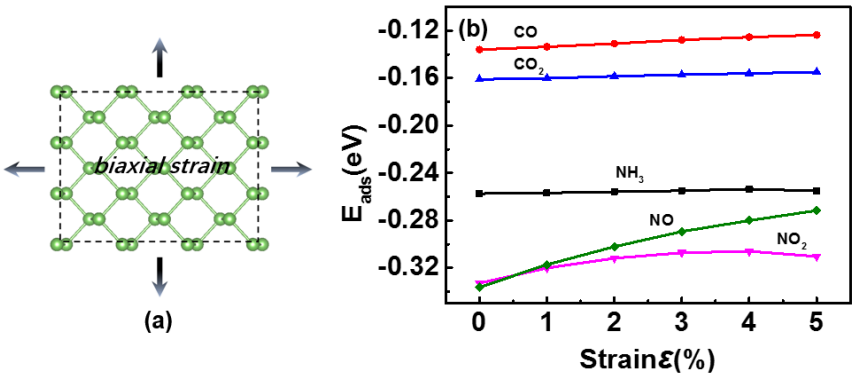

Figure 4 (a) Schematic of B-As under equiaxial tensile strain; (b) adsorption energies of gas molecules (including NH_3, CO, CO_2, NO, and NO_2) as a function of applied biaxial strain. The strained nanosheet has a lattice constant of $a = (1+\varepsilon) \times a_o$.

Previous work uncovered that the gas adsorption strength can be tuned by applying a vertical electric field (*E* field) or strain [43, 44]. Herein, out-of-plane *E* fields and in-plain equibiaxial tensile strains are applied to evaluate the adsorption properties of gas on B-As. Figure 3 (a) shows that the interaction strength of NO and NO_2 with the substrate increases obviously with the *E* field varying from -0.5 V/ Å to 0.5 V/ Å, which may be attributed to the significant increase in charge transfer from the substrate to NO and NO_2, as shown in Figure 3(b). The binding strengths of CO and CO_2 show no significant increase with nearly constant charge transfer (see Figure 3(b)) under the *E* field. Interestingly, desorption of NH_3 occurs under a positive 0.5 V/Å *E* field, and NH_3 undergoes a transition from an electronic donor to an acceptor, as illustrated in Figure 3(b). Tunable adsorption strength makes B-As a promising wide-range application sensor. In contrast, applying in-plane tensile strain induces a slight decrease in the binding strength of these gas molecules, as shown in Figure 4 (b), except for NO_2, which shows a non-monotonic behaviour.

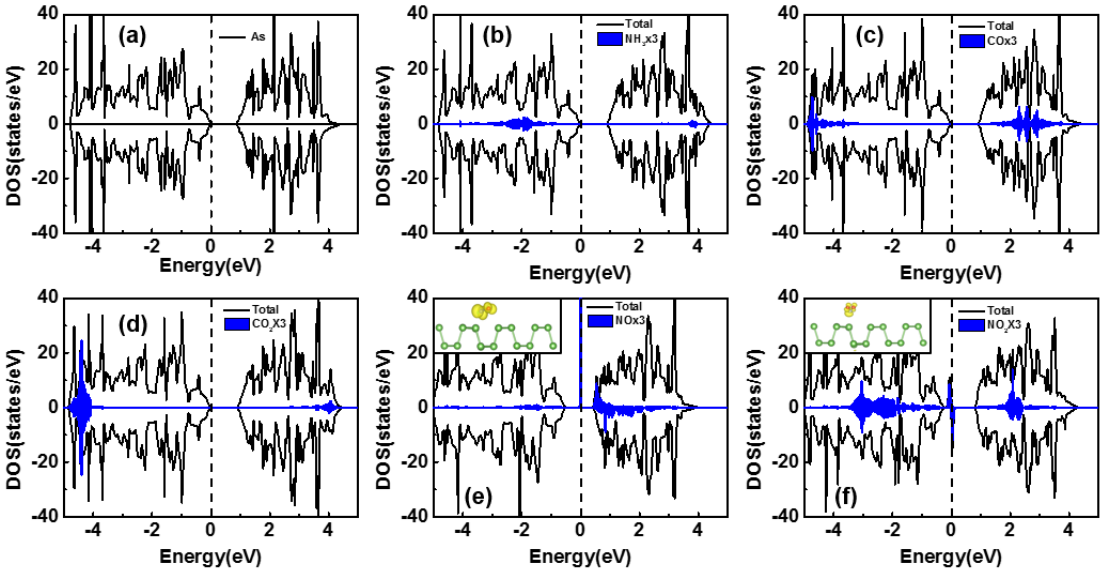

Figure 5 (colour online) (a-e) TDOS of B-As without or with gas molecule adsorption (black curves) and the LDOS projected on gas molecules (blue areas; note that the value of LDOS is enlarged by a scale factor of 3). The insets in (e) and (f) represent the spatial spin density distribution on NO and NO_2 molecules, respectively, with an isovalue of 0.003 e $Å^{-3}$. The Fermi level is shifted to zero and indicated by the vertical dashed lines.

Previous studies have shown that gas adsorption can obviously influence the electronic properties of 2D materials and may induce magnetism [17, 25]. To further examine the influence of gas adsorption on the electronic properties of B-As, the total density of states (TDOS) of B-As and the local density of states (LDOS) projected on NH_3, CO, and CO_2 are shown in Figure 5(b-d); moreover, their corresponding spin polarized band structures are illustrated in Figure S2 (b-d). The DOS for either the valence or conduction bands of B-As is not significantly influenced upon NH_3 adsorption, as shown in Figure 5 (b) and Figure S2 (b). Moreover, the adsorption of CO or CO_2 induces distinct states in the lower valence bands at approximately -4.5 eV; however, no noticeable modifications of the DOS near the Fermi level are observed. In contrast, the adsorption of NO or NO_2 induces significant magnetism (see Table 1), which is also manifested in the spin polarized DOS, as shown in Figure 5 (e, f), and the spin polarized band structures, as depicted in Figure S2 (e, f). From the distribution of spin density shown in the insets of Figure 5(e, f), it is obvious that the magnetization is mainly located on the NO or NO_2 molecules.

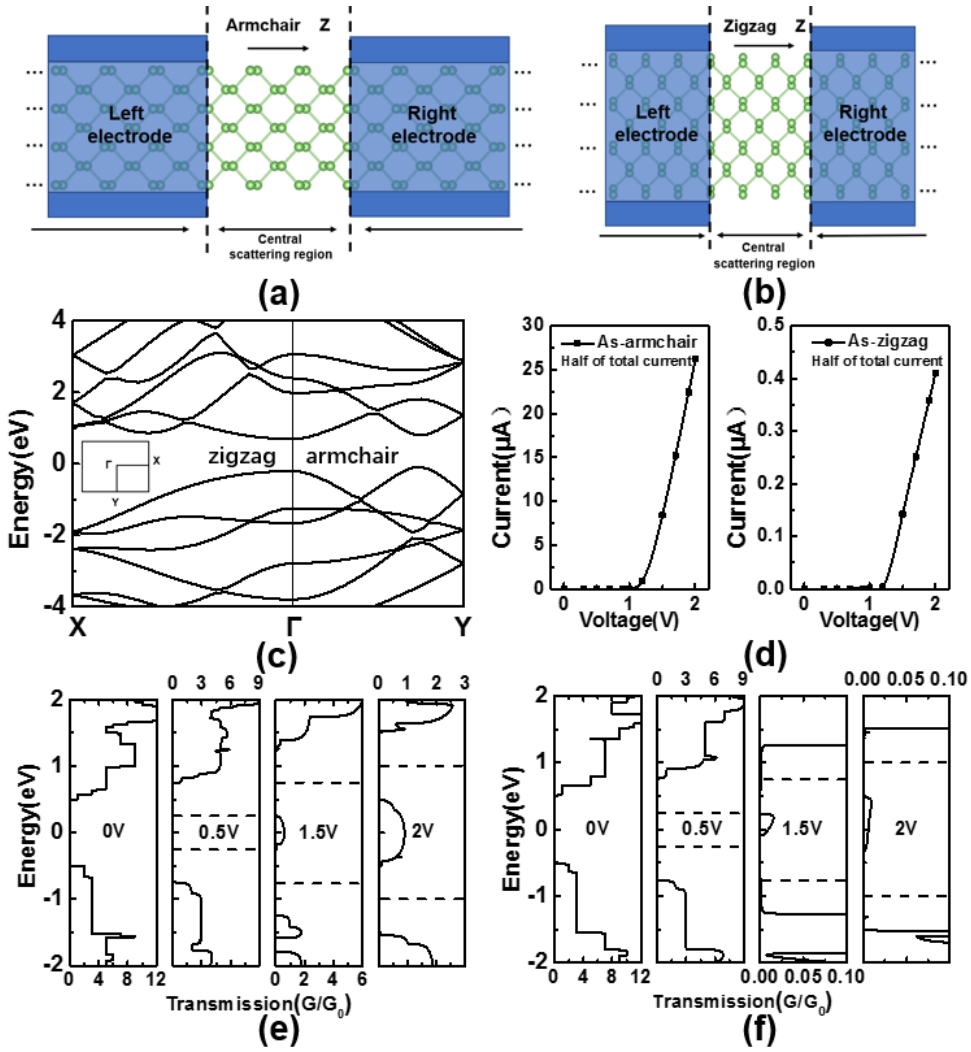

Figure 6 (colour online) (a,b) Schematics of the two-probe systems where semi-infinite left and right electrode regions (blue shaded region) are in contact with the central scattering region along the armchair or zigzag direction. For the electrodes and scatter regions, 3×3 supercells of B-As are used, similar to the models used in ref. [17]. (c) Band structure of B-As calculated using a primitive unit cell. (d) *I*-*V* plots (note that the current here is just half of the total current) of B-As for a bias voltage from 0 to 2 V along the armchair (left) and zigzag (right) directions. Transmission spectral evolution under different bias voltages along the armchair (e) and zigzag (f) directions; dash horizontal lines indicate the bias windows. Fermi energy is set to 0 eV.

Although the electronic structure of B-As after the adsorption of NH_3, CO, or CO_2 does not substantially change, the adsorption-induced charge transfer is expected to affect the resistivity of the system, which can also be measured experimentally and act as an indicator for gas sensors. To explicitly evaluate the performance of B-As as a gas sensor, we employed the NEGF method to calculate the transport transmission and the corresponding *I*-*V* relation before and after gas molecule adsorption. The *I*-*V* relation allows monitoring of the resistivity change and may be

directly compared to the experimental measurements. Due to the structural anisotropy of B-As, two transport models were constructed: one has the current flowing along the armchair direction, as shown in Figure 6 (a), and the other has the current flowing along the zigzag direction, as shown in Figure 6 (b). Normally, the electrical transport properties of 2D materials mostly depend on their band alignments from the inter- and intra-band transitions near the Fermi level [38]. For one thing, only the electrons in the states within the bias window can make effective contributions to the current [45]; for another, the band characteristics, such as the projection of the bands [46] and the parity limitation [47], also have a significant effect on the electrical transport.

To provide an intuitive understanding of the transport phenomena, the electronic band structure of monolayer B-As is given in Figure 6 (c). The bands are anisotropic and more dispersive along the Γ-Y direction (i.e., smaller effective mass), which is the armchair direction in real space; on the other hand, heavier bands are observed along Γ-X, which is the zigzag direction. This means that the charge carrier can be more easily driven along the armchair direction, which is in good agreement with the experimental results of Chen et al. [27] and the theoretical results of Zhong et al. [28]. This directly leads to the anisotropic *I*-*V* curves with a ratio of current anisotropy $\eta = I_{zigzag}/I_{armchair}$ of approximately 65 under a bias voltage of 2 V, as shown in Figure 6 (d). The calculated zero-bias (0 V) transmission spectra along two directions are given in Figure 6 (e) and (f), which apparently mimic the band structures. Likewise, the step-like behaviour of the spectrum is related to the available conductance channels [17, 48]. In Figure 6 (e, f), the transmission spectra at bias voltages of 0.5, 1.5, and 2 V are also presented. As the bias voltage increases, non-zero transmission spectra emerge around the Fermi level in the bias window, which leads the current flow through [45]. Similar *I*-*V* curves were obtained for the adsorption of NH_3, CO, or CO_2 on B-As, as shown in Figure S3.

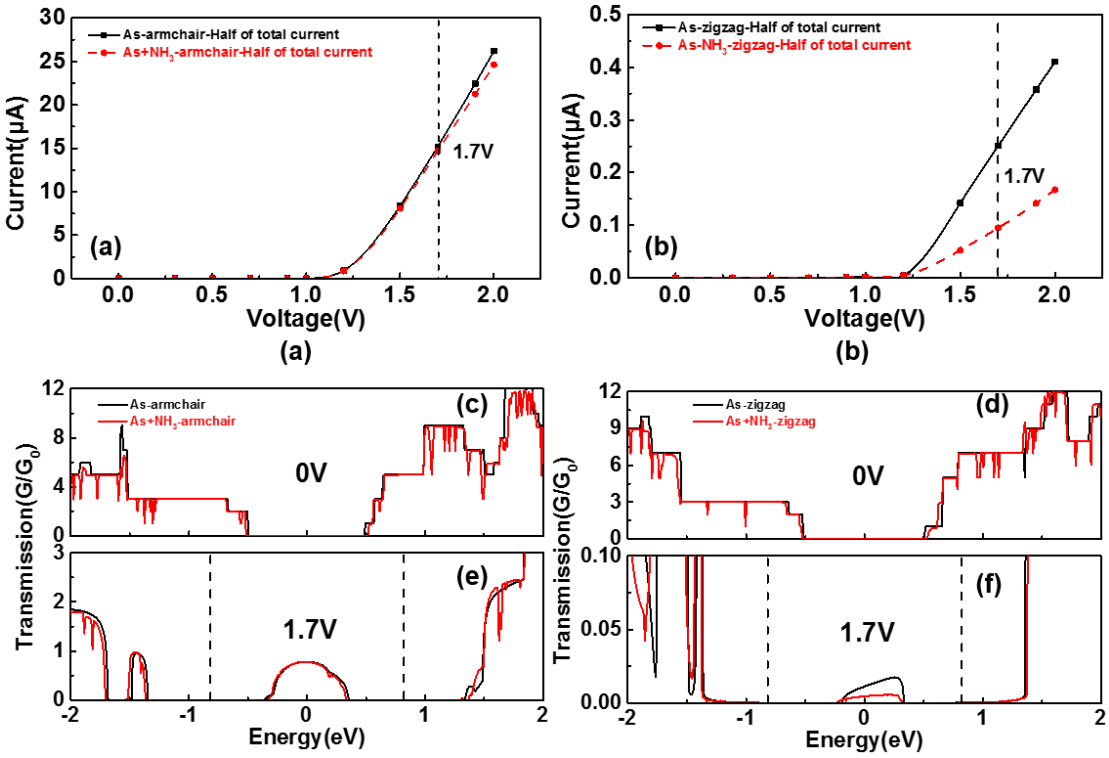

Figure 7 (colour online) The *I-V* curves of B-As without and with NH_3 adsorption along the armchair (a) and zigzag (b) directions. The transmission spectra without and with NH_3 adsorption under zero and 1.7 V bias voltages along the armchair (c, e) and zigzag (d, f) directions.

The sensor performance can be evaluated by the sensor response (*S*). Here, *S* is defined by the relative resistance change as $S = [|R-R_0|/R_0]\times100\%$, where R_0 and R are the resistance of the substrate without and with gas molecules, respectively [49]. As shown in Figure 7 (a), there is a current decrease from 26.20 to 24.61 μA under a bias of 2 V with a response *S* of 6.4% after the adsorption of NH_3 along the armchair direction, indicating an increase in resistance. In contrast, the current drops more significantly, achieving a response S of 141.2% under a bias of 2 V along the zigzag direction. To gain further understanding of the current suppression, the bias-dependent transmission spectra before and after NH_3 adsorption are illustrated in Figure 7 (c-f). It is known that current is mainly attributed to the transmission coefficient around the Fermi level within the bias window [45]. At 1.7 V bias voltage, effective conductance channels in the bias window are inhibited by NH_3 adsorption, leading to the reduction in current. In other words, NH_3 adsorption introduces backscattering centres that reduce available conductance channels, yielding a reduced current. The decreased conductance is more significant along the zigzag

direction, as shown in Figure 7 (f), compared with the armchair direction shown in Figure 7 (e).

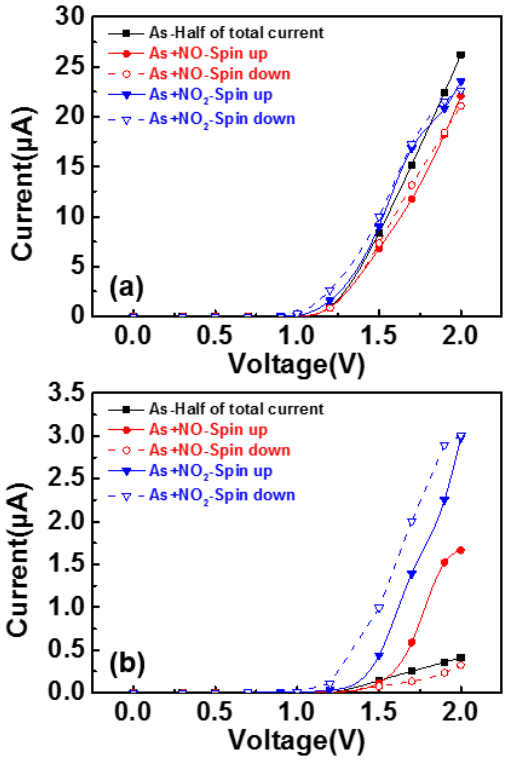

Figure 8 (colour online) Spin polarized *I-V* plots of B-As without and with NO or NO_2 adsorption along the armchair (a) and zigzag (b) directions.

The adsorption of paramagnetic molecules NO and NO_2 on B-As induces spin polarization as indicated above, which leads to spin polarized current and transmission spectra along both the armchair and zigzag directions, as illustrated in Figure 8 and Figure S4. For the spin polarized *I-V* curves along the armchair direction, as given in Figure 8 (a), there is a current reduction after the adsorption of NO, similar to the case of NH_3, but more sensitive (a 18.7% response *S* for the spin up current and a 24.2% response *S* for the spin down current at a bias of 2 V). In contrast, the adsorption of NO_2 induced a current increase before the bias voltage reached approximately 1.8 V. As the bias voltage further increases, the spin up and down currents decrease after the adsorption of NO_2. Current flow along the zigzag direction shows a sharp contrast to the armchair direction, as illustrated in Figure 8 (b). Both spin up and down currents increase significantly with increasing bias voltage after the adsorption of NO_2. A response *S* of 86.3% is obtained under a bias of 2 V for both spin up and down currents. On the other hand, there is a sharp increase in the spin up current with *S* of 75.3% after the adsorption of NO, while

a spin down current reduction with *S* of 27.3% is observed under a bias of 2 V. The very different spin up and down currents not only make B-As a selective sensor for NO but also a promising spin filter [50]. The various responses of the *I-V* curves of B-As induced by different gas molecules suggest wide-range gas sensing applications.

Conclusion

In summary, using first-principles calculations combined with NEGF, we systematically studied the structural, electronic, and transport properties of monolayer black arsenic (B-As) with adsorbed gas molecules, i.e., NH_3, CO, CO_2, NO, or NO_2. Our results show that nitrogen-containing gas molecules have a relatively strong adsorption strength, suggesting that B-As is more sensitive to these gas molecules. This behaviour is attributed to the more sensitive charge transfer induced by the adsorption of NO and NO_2 molecules. Moreover, the binding strength of nitrogen-containing gas molecules can be effectively modulated by a vertical electric field, but it is insensitive to equibiaxial tensile strains. Transport calculations indicate that the adsorption-induced current variation of B-As exhibits strong anisotropic character along the armchair or zigzag directions. The gas molecule adsorption on B-As can either reduce or increase the resistance, which can be directly measured experimentally. Along the zigzag direction, a significant spin polarized current is discovered for the adsorption of NO. Such sensitivity and selectivity to gas molecule adsorption make B-As a promising candidate for gas sensors.

†Electronic supplementary information (ESI) available: Potential adsorption configurations before and after structural optimization; spin-polarized band structures of B-As without and with adsorbates; *I-V* curves of B-As without and with the adsorption of NH_3, CO, or CO_2, and spin-polarized transmission spectra of B-As without and with adsorbed NO and NO_2 under 0 and 1.7 V bias voltages along the armchair and zigzag directions. **See DOI:**

CONFLICTS OF INTEREST

There are no conflicts to declare.

ACKNOWLEDGEMENTS:

This work is supported by the Research Grants Council of Hong Kong (17300018

and 17201019), Environment and Conservation Fund (69/2018), and Science, Technology and Innovation Commission of Shenzhen Municipality (JCYJ20180307154619840). The authors are grateful for the research computing facilities offered by ITS, HKU.

Reference:

1. F.-G. Banica, *Chemical sensors and biosensors: fundamentals and applications*, John Wiley & Sons, 2012.
2. A. De Marcellis and G. Ferri, *Analog circuits and systems for voltage-mode and current-mode sensor interfacing applications*, Springer Science & Business Media, 2011.
3. K. S. Novoselov, A. K. Geim, S. V. Morozov, D. Jiang, Y. Zhang, S. V. Dubonos, I. V. Grigorieva and A. A. Firsov, *Science*, 2004, **306**, 666-669.
4. N. KS, J. D, S. F, B. TJ, K. VV, M. SV and G. AK, *Proc. Natl. Acad. Sci. U S A*, 2005, **102**, 10451-10453.
5. M. Chhowalla, H. S. Shin, G. Eda, L. J. Li, K. P. Loh and H. Zhang, *Nat. Chem.*, 2013, **5**, 263-275.
6. X. Xu, W. Yao, D. Xiao and T. F. Heinz, *Nat. Phys.*, 2014, **10**, 343-350.
7. B. Liu and K. Zhou, *Prog. Mater. Sci.*, 2018, **100**, 99-169.
8. Z. Meng, R. M. Stolz, L. Mendecki and K. A. Mirica, *Chem. Rev.*, 2019, **119**, 478-598.
9. S. Ma, D. Yuan, Y. Wang and Z. Jiao, *J Mater. Chem. C*, 2018, **6**, 8082-8091.
10. F. Schedin, A. Geim, S. Morozov, E. Hill, P. Blake, M. Katsnelson and K. Novoselov, *Nat. Mater.*, 2007, **6**, 652.
11. S. Zhang, M. Xie, F. Li, Z. Yan, Y. Li, E. Kan, W. Liu, Z. Chen and H. Zeng, *Angew. Chem. Int. Ed.*, 2016, **128**, 1698-1701.
12. L. Han, A. T. Neal, Z. Zhen, L. Zhe, X. Xianfan, T. David and P. D. Ye, *ACS Nano*, 2014, **8**, 4033-4041.
13. O. U. Akturk, V. O. Özçelik and S. Ciraci, *Phys. Rev. B*, 2015, **91**, 235446.
14. E. Aktürk, O. Ü. Aktürk and S. Ciraci, *Phys. Rev. B*, 2016, **94**, 014115.
15. A. A. Kistanov, Y. Cai, D. R. Kripalani, K. Zhou, S. V. Dmitriev and Y.-W. Zhang, *J Mater. Chem. C*, 2018, **6**, 4308-4317.
16. D. Singh, S. K. Gupta, Y. Sonvane and I. Lukačević, *J Mater. Chem. C*, 2016, **4**, 6386-6390.
17. L. Kou, T. Frauenheim and C. Chen, *J. Phys. Chem. Lett.*, 2014, **5**, 2675-2681.
18. A. N. Abbas, B. Liu, L. Chen, Y. Ma, S. Cong, N. Aroonyadet, M. Köpf, T. Nilges and C. Zhou, *ACS nano*, 2015, **9**, 5618-5624.
19. S. Cui, H. Pu, S. A. Wells, Z. Wen, S. Mao, J. Chang, M. C. Hersam and J. Chen, *Nat. Commun.*, 2015, **6**, 8632.
20. G. Wang, W. J. Slough, R. Pandey and S. P. Karna, *2D Mater.*, 2016, **3**, 025011.
21. A. Ziletti, A. Carvalho, P. Trevisanutto, D. Campbell, D. Coker and A. C. Neto, *Phys. Rev. B*, 2015, **91**, 085407.
22. F. Safari, M. Moradinasab, M. Fathipour and H. Kosina, *Appl. Surf. Sci.*, 2019, **464**, 153-161.
23. T. Lei, C. Liu, J. L. Zhao, J. M. Li, Y. P. Li, J. O. Wang, R. Wu, H. J. Qian, H. Q. Wang and K.

Ibrahim, *J. Appl. Phys*, 2016, **119**, 1757-1761.
24. H. S. Tsai, S. W. Wang, C. H. Hsiao, C. W. Chen, H. Ouyang, Y. L. Chueh, H. C. Kuo and J. H. Liang, *Chem. Mater.*, 2016, **28**,.
25. C. Liu, C.-S. Liu and X. Yan, *Phys. Lett. A*, 2017, **381**, 1092-1096.
26. C. Kamal and M. Ezawa, *Phys. Rev. B*, 2014, **91**, 849-855.
27. Y. Chen, C. Chen, R. Kealhofer, H. Liu, Z. Yuan, L. Jiang, J. Suh, J. Park, C. Ko and H. S. Choe, *Adv. Mater.*, 2018, **30**, 1800754.
28. M. Zhong, Q. Xia, L. Pan, Y. Liu, Y. Chen, H. X. Deng, J. Li and Z. Wei, *Adv. Funct. Mater.*, 2018, **28**, 1802581.
29. S. Mardanya, V. K. Thakur, S. Bhowmick and A. Agarwal, *Phys. Rev. B*, 2016, **94**, 035423.
30. Y. Sun, W. Dong and Z. Shuai, *J Phys. Chem. C*, 2017.
31. J. Mao and Y. Chen, *Phys. Chem. Chem. Phys.*,2019, **44**, 24499-24505.
32. L. Kou, Y. Ma, X. Tan, T. Frauenheim, A. Du and S. Smith, *J Phys. Chem. C*, 2015, **119**, 6918-6922.
33. G. Kresse, *Comput. Mater. Sci.*, 1996, **6**, 15.
34. G. Kresse and J. Furthmüller, *Phys. Rev. B*, 1996, **54**, 11169.
35. S. Grimme, *J Comput. Chem.*, 2006, **27**, 1787-1799.
36. G. Henkelman, A. Arnaldsson and H. Jónsson, *Comp. Mater. Sci.*, 2006, **36**, 354-360.
37. M. Brandbyge, J.-L. Mozos, P. Ordejón, J. Taylor and K. Stokbro, *Phys. Rev. B*, 2002, **65**, 165401.
38. S. Datta, *Electronic transport in mesoscopic systems*, Cambridge university press, 1997.
39. F. K. Perkins, A. L. Friedman, E. Cobas, P. Campbell, G. Jernigan and B. T. Jonker, *Nano Lett.*, 2013, **13**, 668-673.
40. S. Zhao, J. Xue and W. Kang, *Chem. Phys. Lett.*, 2014, **595**, 35-42.
41. Y. Cai, Q. Ke, G. Zhang and Y.-W. Zhang, *J Phys. Chem. C*, 2015, **119**, 3102-3110.
42. O. Leenaerts, B. Partoens and F. Peeters, *Phys. Rev. B*, 2008, **77**, 125416.
43. X.F. Yu, Y.C. Li, J.B. Cheng, Z.B. Liu, Q.Z. Li, W.Z. Li, X. Yang and B. Xiao, *ACS Appl. Mater. Interfaces*, 2015, **7**, 13707-13713.
44. T. Zhang, Q. Xue, M. Shan, Z. Jiao, X. Zhou, C. Ling and Z. Yan, *J Phys. Chem. C*, 2012, **116**, 19918-19924.
45. Z. Ni, H. Zhong, X. Jiang, R. Quhe, G. Luo, Y. Wang, M. Ye, J. Yang, J. Shi and J. Lu, *Nanoscale*, 2014, **6**, 7609-7618.
46. Y. An, J. Jiao, Y. Hou, H. Wang, R. Wu, C. Liu, X. Chen, T. Wang and K. Wang, *J. Phys. Condens. Matter*, 2018, **31**, 065301.
47. Z. Li, H. Qian, J. Wu, B.-L. Gu and W. Duan, *Phys. Rev. Lett*, 2008, **100**, 206802.
48. M. Topsakal, V. Bagci and S. Ciraci, *Physical Review B*, 2010, **81**, 205437.
49. K. Lee, R. Gatensby, N. McEvoy, T. Hallam and G. S. Duesberg, *Adv Mater*, 2013, **25**, 6699-6702.
50. J. Huang, K. Xu, S. Lei, H. Su, S. Yang, Q. Li and J. Yang, *J. Chem. Phys.*, 2012, **136**, 064707.